Imperial College
London

Department of Physics
High Energy Physics Research Group
July 2022

Development of an ion-acoustic dose-deposition mapping system for LhARA

PhD Early Stage Assessment Report

Author: Maria Maxouti
Supervisor: Kenneth Long

Abstract

The Laser-hybrid Accelerator for Radiobiological Applications, LhARA, has been proposed as a facility dedicated to the study of radiation biology. An on-the-fly, non-invasive, range verification system needs to be developed that would provide a quantitative 4D dose deposition profile and Bragg peak localization for pre-clinical research and, at a later stage, provide clinical measures of the Bragg peak and deposited energy distribution within tissue. This work focuses on the development of an experiment to demonstrate the feasibility of ion-acoustic imaging, which is based on ion-induced ultrasound waves, to provide the energy-deposition profile of ion beams propagating in a medium. Different image reconstruction techniques are also investigated and their performance are evaluated using Geant4 and k-Wave.

Contents

1 Introduction

Cancer is the second most common cause of death globally [1]. In 2018, around 17 million new cancer cases were diagnosed and around 9.6 million people died worldwide [2]. These numbers are estimated to increase in the next few years, therefore it is crucial to provide patients with effective treatment and prevent the loss of life. Novel, cost-effective and efficient techniques need to be incorporated into treatment facilities, accessible to the wider population irrespective of socioeconomic status.

1.1 Radiotherapy

Radiotherapy is a clinical therapy that uses ionising radiation to treat tumours by controlling or killing malignant cells that proliferate [3]. It is used to treat over 50% of the cancer patients [2], often in parallel to chemotherapy and surgical removal. Despite the treatment being highly successful, there are several drawbacks to this treatment modality, with the most imminent ones revolving around the effect of ionising radiation on healthy host cells surrounding the cancerous growths.

Radiotherapy aims to give a defined radiation dose to the patient, targeted at the tumour area. The radiation is absorbed by the cancerous cells and the DNA breaks up and stops reproducing [3]. This causes the excessive replication of the cell to stop and it eventually becomes benign (non-cancerous). By falsely irradiating the surrounding healthy tissue, there is a high risk of additional tumours being formed, called carcinogenesis, highlighting the importance of effective targeting.

The most common form of radiotherapy uses x-rays, but although photons are highly effective they don't deposit most of their energy in the tumour area but along the entire path. Because of this, protons and light ions are currently considered to be used in the development of new cancer treatment facilities, as they can deposit most of their energy in a small volume of tissue [4]. This is because as the ions interact with the tissue, they slow down and hence they are able to deposit more energy in a shorter range and time. The maximum deposition is observed as a sharp peak, called the Bragg peak, and hence the effect on the healthy tissue surrounding it is minimized [5]. A comparison of the dose delivery as a function of distance for each method is illustrated in Figure 1. The dose is usually measured in Gray (Gy), where 1 Gray is the absorption of one joule of radiation energy per one kilogram of matter [6]. Moreover, as can be seen from Figure 1, there is an entrance delivery dose before the peak. This can be decreased by using light-ion beams, however, there is the drawback of a fragmentation tail beyond the Bragg peak region. This is highly unwanted, especially in the case where vital organs are located behind the tumour that can be severely damaged.

1.2 Energy loss & Linear Energy Transfer (LET)

The mean energy loss of a particle as a function of distance travelled within a medium is described by the Bethe-Bloch formula. This formula is defined in Equation 1.1, where E is the particle's energy, x the distance travelled, Z the atomic number of the element in the medium, A the mass number of the element in the medium, z the incident particle charge,

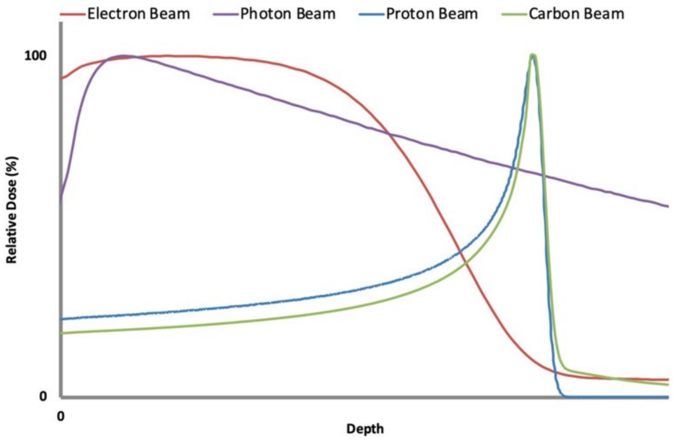

Figure 1. Relative dose deposition profile for electrons (red), photons (purple), protons (blue) and carbon ions (green) [5].

I the mean excitation energy, γ the Lorentz factor, β the ratio of the particle's velocity to the speed of light i.e. $\beta = \frac{v}{c}$ and $\delta(\beta\gamma)$ the density effect correction due to polarisation [7]. K and T_{max} (the maximum kinetic energy transferred) are defined in Equations 1.2 & 1.3 , where N_A is the Avogadro constant, r_e the electron radius, m_e is the electron mass and m_0 the mass of the incident particle.

$$-\langle\frac{dE}{dx}\rangle = Kz^2\frac{Z}{A}\frac{1}{\beta^2}[\frac{1}{2}ln(\frac{2m_ec^2\beta^2\gamma^2T_{max}}{I^2}) - \beta^2 - \frac{\delta(\beta\gamma)}{2}] \tag{1.1}$$

$$K = 4\pi N_A r_e^2 m_e c^2 \tag{1.2}$$

$$T_{max} = \frac{2m_ec^2\beta^2\gamma^2}{1 + \frac{2\gamma m_e}{m_0} + (\frac{m_e}{m_0})^2} \tag{1.3}$$

When a particle propagates within a patient during treatment, this energy loss is mostly deposited in the tissue, therefore it is common to refer to this as the Linear Energy Transfer (LET). LET is the average energy transferred per unit length [8]. LET is similar to the stopping power, but it does not consider nuclear interactions. Each type of particle is associated with a different value, and generally, photon and proton beams have a low-LET, while heavy ions have a high-LET around the Bragg peak region. A high LET value has several biological advantages, such as more significant DNA damage and suppression of radiation repair [8].

1.3 Relative Biological Effectiveness (RBE)

The Relative Biological Effectiveness (RBE) defines the biological effect of one type of ionizing radiation relative to another, and it critically depends on both physical and biological parameters such as type of radiation, LET, dose, dose rate, target cell, radiosensitivity etc [9]. The RBE value can be used to compare hadron therapy and conventional photon therapy that is better understood. A comparison of the biological effect caused by the hadron dose can be compared to the photon dose required to produce the same effect. Typically, tissues that can repair a large amount of damage caused by radiation have a high RBE value. A table of some typical RBE values for different radiation types, in comparison to a reference photon beam, is shown in Table 1 [10]. Taking values from the table as an example, using a proton beam with RBE of 1.1 means that the patient will receive a 10% lower dose compared to a treatment using photons, for the same effect.

Radiation quality	Typical RBE
250 kV X-rays	1.0
MV X-rays	1.0
electrons	1.0
protons	1.1-1.5
$C^{6+} ions$	1.5-5
fast neutrons	4-5

Table 1. Typical Relative Biological Effectiveness (RBE) values for different radiation types, in comparison to a reference photon beam [10].

In addition, ions with very high LET around the Bragg peak, lead to significant uncertainties in the RBE value. Such uncertainties can lead to incorrect dose estimations and extensive damage to healthy cells. Furthermore, ions with different RBE values induce different damages to the DNA, where the higher the value, the greater the damage.

1.4 Medical Imaging

Medical imaging is used to diagnose and monitor medical conditions using several different technologies [11]. In general, imaging is limited by spatial resolution (a measure of the smallest object that can be resolved), signal-to-noise ratio (ratio between the power of the desired and undesired signal) and contrast-to-noise ratio (coming from noise sources such as clutter and speckle) that determines the image quality [11]. Noise could be in the form of acoustic noise, electrical noise or ion pulse variations. Because of these, acoustic imaging is considered to be better than optical imaging because it is not limited by depth and spatial resolution, as acoustic waves are scattered much less than photons in tissue [12].

1.4.1 Ultrasound

Ultrasound is a mechanical longitudinal wave and it is widely used in today's clinical imaging systems [13]. As the ultrasound waves travel through tissue, some of them are reflected between boundaries (or small structures within a homogeneous tissue) with different acoustic and physical properties. The back-scattered waves can be detected by a transducer (consisting of an array of multiple transducer elements) and the time between pulse transmission and signal reception can be used to calculate the depth of the tissue boundary. This can be repeated many times until an image is acquired, where the intensity of each pixel is proportional to the strength of the back-scattered signal. Generally, signals received from boundaries deeper in the body appear to be weaker than those reflected at boundaries closer to the surface. Due to the extremely high speed of the ultrasound wave in tissue, real-time imaging can be performed in a few seconds [13].

1.4.2 Photo-acoustic Imaging

Photo-acoustic imaging is a non-invasive modality that uses ultrasound pulses created by a pulsed laser [14]. As the laser beam penetrates the tissue, it is scattered and absorbed by different chromophores (e.g. melanin and haemoglobin), which are parts of a molecule responsible for its colour. As the energy is absorbed, the temperature increases which results in thermoelastic expansion. This leads to an increase in pressure and an acoustic wave is emitted (thermoacoustic effect), with the emitted pressure wave's amplitude, frequency and shape being dependent on the dielectric properties of the tissue. These emitted acoustic waves can be detected by a transducer and be used in image reconstruction [14]. The whole principle is illustrated in Figure 2 [15].

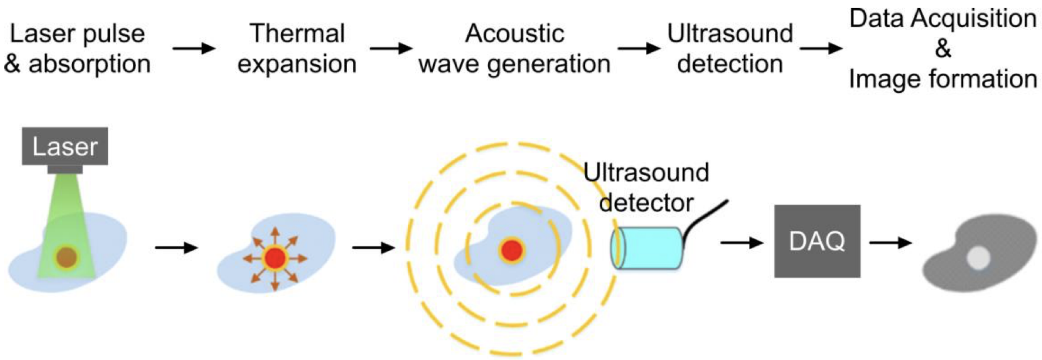

Figure 2. An illustration of the photo-acoustic effect, from signal generation until image reconstruction [15].

1.4.3 Ion-acoustic Imaging

Ion-acoustic imaging works similarly to photo-acoustic imaging, but the induced acoustic waves are produced by proton or ion energy depositions. As the ion-beam propagates through the tissue it interacts via Coulomb interactions and transfers its kinetic energy to the cells in the form of heat. This results in thermoelastic expansion and a local pressure increase which results in the emission of a shear ion-acoustic pressure wave. These induced ion-acoustic waves are dependent on the energy and width of the beam, which also influence the shape of the Bragg peak that is the most predominant source of the waves. Therefore, the shape of this pressure wave carries all the information about the spatial and temporal characteristics of the source causing it. In addition, thermal diffusion can be neglected during this process as the rate of heat deposition is extremely fast - of the order of picoseconds - much faster than the time needed for the ions to stop.

Furthermore, since ion-acoustic waves observed in clinical applications suffer from low-pressure amplitudes ($\sim$ mPa) and low-frequencies ($\sim$ kHz), ion-acoustic detection is very challenging and therefore there is a need to find ways by which the signals can be enhanced so that the system can be integrated for clinical and pre-clinical applications. Moreover, one of the drawbacks of this technique is that it suffers from low signal-to-noise ratio (SNR) and hence detectors with high sensitivity are required.

Both photo-acoustic and ion-acoustic imaging can be used to obtain a quantitative dose distribution of the beam, and provide a direct Bragg peak position measurement, with submillimeter accuracy. The research done up to now is discussed in Section 4.

2 The Laser-hybrid Accelerator for Radiobiological Applications

The Laser-hybrid Accelerator for Radiobiological Applications (LhARA) aims to demonstrate technologies that can enhance the clinical application of radiotherapy [16]. It envisages to use protons and light ions instead of photons, allowing research in radiobiology and particle-beam therapy to be delivered in new a regimen and exploit ultra-high dose rates. A wide variety of time structures, spectral distributions and spatial configurations can be used in a flexible way, thus instantaneous dose rates beyond the ”FLASH” regime (≥ 40 Gy/s) can be delivered [17], the therapeutic effect of which can be studied. Such instantaneous dose rates can potentially offer a more effective therapy and reduce the duration of the treatment. LhARA will potentially provide a facility which is significantly smaller, cheaper and more flexible with an extended range of beam characteristics. The LhARA accelerator is designed in such a way as to provide different end stations, initially 10–15 MeV in vitro (allowing radiobiological studies), and then after using fixed-field alternating-gradient acceleration, reach in vitro and in vivo stations with proton beam energies of up to 127 MeV or ions up to 33 MeV per nucleon. A schematic diagram of the LhARA beamlines is shown in Figure 3.

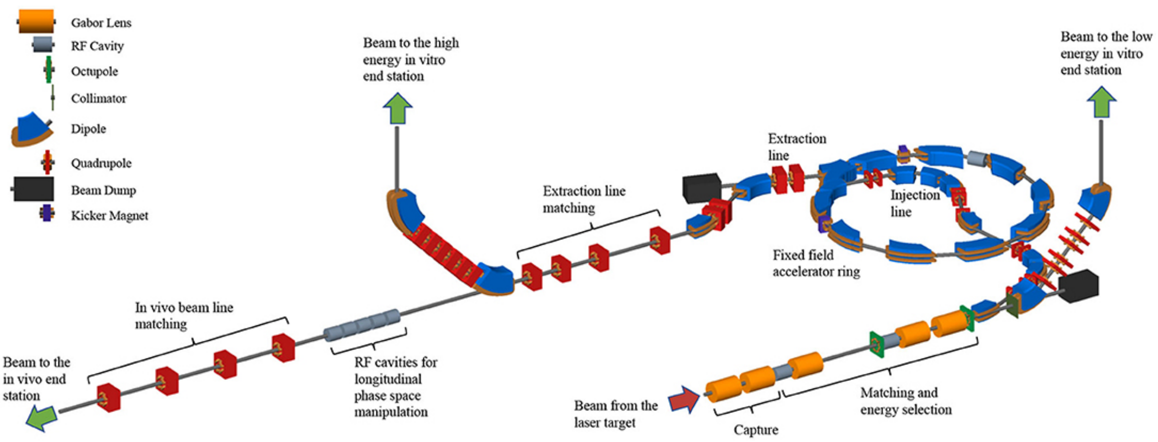

Figure 3. Schematic diagram of the LhARA beamlines [16].

3 Forming a proof of principle for LhARA

As mentioned in Section 1.1, ions provide a more advantageous energy dose distribution within tissue compared to photons, due to their ability to deposit a maximum dose at the end of their range. This property is favourable as it enables selective treatment while sparing the healthy cells around the tumors. But the Bragg peak position within the patient must be accurately monitored. An on-the-fly, non-invasive, range verification system needs to be developed, for LhARA, that would provide a quantitative 4D dose deposition profile and Bragg peak localization for pre-clinical research and, at a later stage, provide clinical measures of the Bragg peak deposited energy distribution in tissue. The on-the-fly range verification system will also minimize delivery uncertainty and enable a more reliable, aggressive, real-time pulse-to-pulse adaptive treatment plan.

As discussed in Section 1.4.3, ion-acoustic imaging, which is based on ion-induced ultrasound waves, is a promising technique to provide a fast ion beam profile feedback and act as an innovative diagnostics system. To confirm the fundamental ability of ion-acoustic tomography to provide the beam profile within the required time-frame for LhARA, simulations are currently being developed using Geant4 [18] and Matlab [19]. After proving that the method works using the simulation, an experiment will be performed that would validate the detection method.

3.1 Geant4

Geant4 is a software written in C++ that uses stochastic Monte Carlo techniques for the simulation of the passage of particles through matter. It has several features such as *geometry* for simulating the physical layout of the apparatus, *tracking* for simulating the passage of the particles in the detector, and *detector response* which simulates how a real detector would respond. Geant4 allows the measurement of several parameters, such as momentum, energy, mass and direction of travel.

3.2 SmartPhantom

The SmartPhantom is a proposed instrument composed of a tank filled with water, with a series of scintillating fibre planes inserted within it. Such an instrument can effectively mimic human muscle and soft tissue and can be used to perform experiments as an initial step before proceeding to biopsy samples. The beam can be targeted towards the tank via a small window, and the energy loss as a function of distance can be obtained from the scintillating fibre planes' feedback. The design of the SmartPhantom is discussed later in Section 5.1. From the data, the energy deposition profile can be obtained and the Bragg peak can be located. The data can then be calibrated against dosimetric standards to estimate the exact dosimetry and LET received. Geant4 can be used to simulate the SmartPhantom and obtain the energy loss as a function of distance within it.

3.3 k-Wave

k-Wave is an open-source MATLAB toolbox designed for the simulation of propagating linear and non-linear acoustic waves [20]. It works in the time-domain and can simulate signals in 1D, 2D and 3D, in both homogeneous and heterogeneous media. k-Wave also considers attenuation and reflections and can be used to simulate the ion-acoustic process (increase in temperature, pressure and emission of an acoustic wave), when the ion-beam interacts with the medium.

The linear acoustic wave propagation within a medium can be described by the equation of motion, the continuity equation and the adiabatic equation of state. K-Wave solves these equations numerically by using a pseudo-spectral (PS) method [21]. The PS method fits a Fourier series to all the data and the gradient of the wave field is calculated in the time domain using conventional finite-difference schemes. k-Wave also uses a k-space approach (spatial frequency domain of a spatial, global Fourier transform) which uses larger time-steps, compared to other methods for the same degree of accuracy, and therefore less memory is used which leads to a faster model.

A diagram of how Geant4 and k-Wave can be used to simulate the LhARA proof-of-principle experiment can be seen in Figure 4. From the analysis, the Bragg peak and dosimetric data would be retrieved.

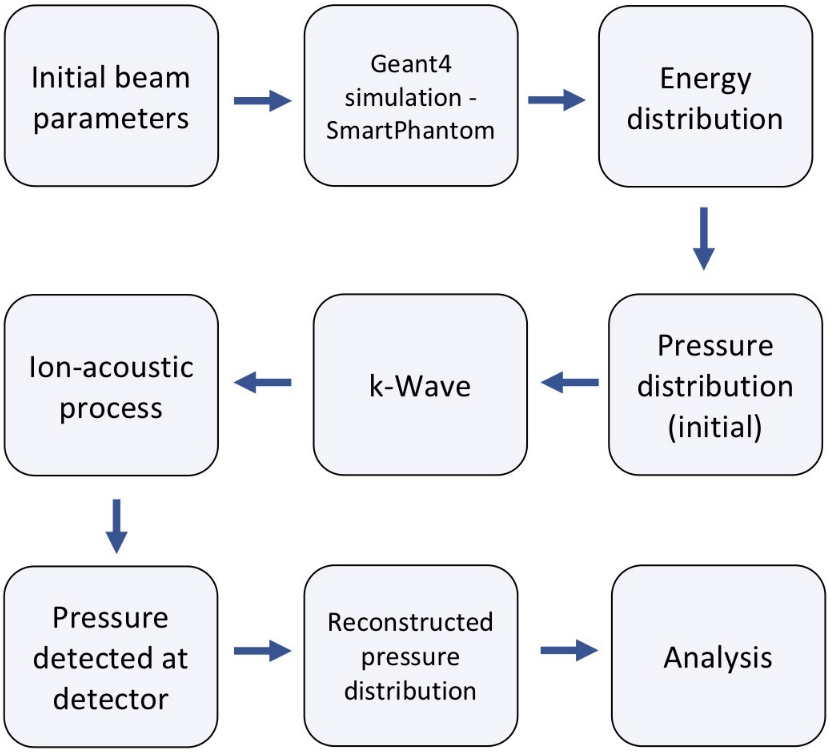

Figure 4. An outline of the LhARA proof-of-principle simulation pipeline, using Geant4 and Matlab's K-Wave tooklit.

3.4 Limitations

The LhARA proof-of-principle experiment has a lot of limitations and differences as to what would happen when treating a patient. Specifically, the tissue is not pure water, but instead contains structures which are hard to simulate in a precise manner. In addition, the fibre planes inserted within the water tank are not present in the human tissue. These planes would influence the results obtained in the proof-of-principle experiment, but would be absent during treatment. This effect is eliminated though at very high energies. In addition, a real patient breathes which causes ion range variations within the body. During respiration, the whole anatomy of the patient changes every second, whereas, in the experiment designed, the SmartPhantom has a fixed size and shape. Anatomical variations can also arise from patient positioning errors (misalignment during treatment setup) and cardiac movements.

Moreover, the ionacoustic imaging technique has several limitations and sources of errors, that arise from non-ideal ion pulses, heterogeneity (a major source of random uncertainties), noise and asymmetric energy depositions. The acoustic signals generated from tissue are also extremely weak and hence large acquisition times are required to detect them. In addition, transducer arrays with hundreds of elements would be needed so that noise can be averaged-out and the signal-to-noise ratio is enhanced. The signal-to-noise ratio per dose can also be improved by reducing the rise time and ion pulse width, which would also produce a sharper Bragg peak.

Furthermore, realistic detectors have limited directionality (field-of-view), limited bandwidth (i.e. a large proportion of the frequency spectrum is lost which might also affect the signal-to-noise ratio) and a frequency-specific phase shift (acoustic and physical center might not coincide, resulting in signal delay). The frequency-specific phase shift can be corrected by measuring the offset experimentally and then adding it in the post-processing for calibration. Solving the limited bandwidth problem will also enhance the signal-to-noise ratio. In addition, by creating compressed sensing flexible transducer array designs with elements that vary in location and center frequency, according to the direction of the wave, would enable the employment of natural frequency variations of the emitted wave. Moreover, the detector system to be used during treatment must permit imaging without disturbing the irradiation. This is a challenging task to overcome and a possible solution is to use a flexible system consisting of inter-communicating sub-arrays with the array configuration being specific for each organ imaged. Care must also be taken when choosing the sensor such that the sensor frequency response does not distort the signal.

4 Literature Review

Before designing, simulating and constructing the proof-of-principle experiment it is important to read and investigate work done by other scientists prior to us. This would enable us to avoid mistakes, identify unknown topics, and develop new ideas which would potentially lead to the development of a fruitful experiment. This literature review specifically focuses on the ion-acoustic imaging techniques developed up to now, as well as the technology used to develop phantoms similar to the one required for our experiment.

4.1 Range Verification Studies

In 2018, an article was published with the title "Acoustic-based proton range verification in heterogeneous tissue: simulation studies" [22]. This article investigates the effect of heterogeneity when using ionacoustics for the localization of the Bragg peak. Specifically, a CT-based simulation method was proposed to model the effect when applying ionacoustics to prostate and liver measurements. A simulation was performed using 124.9-136.3 MeV pulsed proton beams ($\sim$14 μs FWHM), 10^7 protons each and 1.0-1.4 cGy dose at the Bragg peak. The beam dose deposition profiles were calculated (using the Eclipse software [23]) and the acoustic wave propagation was simulated using k-Wave. The results of the simulation were then compared to homogeneous water tank measurements to assess the effect of heterogeneity. The paper concludes that the ionacoustics range verification in a heterogeneous tissue results in decreased pressure amplitudes (by up to 5 times) compared to a homogeneous sample. This can be explained by the fact that elements introducing heterogeneity, such as fat and muscle, generate different ionacoustic waves, different pressure amplitudes for the same energy, and the emitted waves can have different reflectivity, speed and attenuation. In addition, it was observed that the pressure amplitude and range verification accuracy decreased when using longer proton pulses. This study is particularly important as it highlights the difference between experiments where the phantom is homogeneous (such as a water tank) and in vivo experiments where a real tissue is heterogeneous.

In 2021 an article was published with the title "Dictionary-based protoacoustic dose map imaging for proton range verification" [24]. This paper used proton dose distributions from previous studies to create a dictionary of the expected ultrasonic signals. The calculations of the propagation of the acoustic signals until detection point were performed using k-Wave, and it is proposed that this dictionary can be used to match experimental data with the pre-calculated simulated dictionary acoustic signals to map the dose deposition profile. The efficiency of the dictionary was tested using 120-196 MeV proton beams (8.9-10.0 mm FWHM). The paper also suggests that this signal dictionary-based method has the ability to detect alterations such as anatomical changes (tested by inserting air regions and soft tissue regions in the beam's way), within 1.4 mm, while it can also localize the Bragg peak within 1 mm. In addition, this dictionary-based dose reconstruction method requires less computational time, making an in-vivo, on-the-fly, verification range study more feasible.

In 2017 a paper was published with the title "Two-stage ionoacoustic range verification leveraging Monte Carlo and acoustic simulations to stably account for tissue inhomogeneity and accelerator-specific time structure - A simulation study" [25]. This paper introduces a method to estimate the beam range within a medium using "control points" that come from a database of pre-computed thermoacoustic emissions (using k-Wave) and Bragg peak locations. This was done in a two-stage process, where initially, a preliminary range estimate was calculated by the pre-processed emissions, and as a second step, the data were compared to the initial estimate to perform a triangulation of the Bragg peak and refine the range estimate. This method appears to be robust and accurate for low frequency and noisy thermoacoustic emissions, despite high signal-to-noise ratio (SNR) and tissue heterogeneity. The clinically relevant beam range estimates using this method have an average error of 2 mm or less.

In 2019 a paper was published with the title "Simulation studies of time reversal-based protoacoustic reconstruction for range and dose verification in proton therapy" [26]. This paper introduces a 2D time-reversal image reconstruction method for the range and dose verification of a mono-energetic proton pencil beam in heterogeneous tissue. The energy dose depositions were calculated using GATE [27] and the image reconstruction was performed using k-Wave. The effect of sensor number, sampling duration, timestep, noise and number of iterations was also examined. It was observed that increasing the number of sensors improves the range and dose verification accuracy as there is a larger spatial coverage. The same effect was also observed when increasing the sampling duration, which can be explained by the fact that more energy information is included (increasing the sampling duration results in an increase of the measurement aperture). In addition, it was observed that increasing the number of iterations during reconstruction increases the range accuracy. On the other hand, it was observed that increasing the sampling timestep decreases the accuracy of the reconstructed distribution as numerical dispersion is introduced. Moreover, it was observed that noise reduced the reconstruction accuracy as well as introduced instabilities that are observed as large standard deviation values in the Bragg peak localization. One thing addressed by this paper is that the impact of all these parameters on the range verification accuracy is expected to be the same for the 3D case, although more research needs to be done. Generally, it was concluded that the time-reversal technique enables a quantitative Bragg peak localization accuracy below 1 mm, as well as arbitrary geometry, attenuation and heterogeneity detection.

In 2016 a paper was published with the title " Acoustic time-of-flight for proton range verification in water" [28]. The paper uses ionacoustic imaging to characterize the dose and range of a mono-energetic 190 MeV pulsed (17 μs width, 100 Hz pulse repetition frequency) pencil proton beam into a homogeneous water tank. The generated acoustic waves were measured with a hydrophone and the waveforms were compared to simulations to assess the accuracy of the time-of-flight calculations. Using a deconvolution method, the beam position was measured with 2.0 mm accuracy, and the Bragg peak range was measured with -4.5 mm mean in the error distribution and a 2.0 mm standard deviation. These results verify that measurements of the arrival times of thermoacoustic waves, produced by a clinically relevant proton beam, can be used to provide the dose and range. The paper also mentions that synchrocyclotron ion sources may be more favourable than cyclotron ion sources because they can generate shorter pulses (and more protons per pulse) and hence sharper Bragg peaks and higher signal-to-noise ratios per dose.

In 2021, a paper was published with the title "Front-end Design Optimization for Ionoacoustic 200 MeV Protons Beam Monitoring with Sub-millimeter Precision for Hadron Therapy Applications" [29]. The paper introduces a method of improving the signal-to-noise ratio by averaging the acoustic signals received by several sensors, instead of irradiating the patient with multiple beam shots and averaging those. For this purpose, a multichannel sensor has been designed through the development of integrated circuits front-ends. Initially, the Bragg peak localization precision required was used to obtain the required SNR (due to noise and sensor non-idealities this SNR should be slightly larger). A single channel, and then a multichannel, sensor was designed which met the noise, frequency (should match the signal bandwidth) and directionality requirements. Directionality has been reduced by making the sensor much smaller than the acoustic wavelength, which further increases sensitivity and SNR. After making sure that these requirements have been met, the number of channels needed (through averaging) to obtain the required SNR was calculated. The design was tested using a simulation, performed in Geant4 and k-Wave, with a 200 MeV proton beam (19.2 mm FWHM, 35 mGy dose deposition per shot, 7.5 cm BP distance, 25 mPa signal amplitude) and the proposed detector design achieved a 20.5 dB single-shot SNR and Bragg peak localization within 0.5 mm precision. Therefore, multichannel sensors can achieve improved SNR compared to a single-channel sensor, for the same dose deposition. This paper demonstrates that improving the detector design, rather than the post-processing, and averaging in the space domain instead of the time domain can have significant benefits.

4.2 Energy Distribution Measurement Studies

In 2019 a paper was published with the title "I-BEAT: Ultrasonic method for online measurement of the energy distribution of a single ion bunch" [30]. This paper discusses a method by which the kinetic energy distribution of a short ion bunch propagating through water can be quantitatively measured. The proposed technique is called Ion-Bunch energy Acoustic tracing (I-BEAT), and it enables the direct monitoring of a single laser-driven ion bunch at a high repetition rate. To validate the technique, an experiment was performed where the proton bunch entered a cylindrical water tank via a thin aluminium foil. As it propagated through the water, the generated acoustic waves emitted during energy deposition were measured using an on-axis ultrasound 10 MHz transducer. The pressure signal was then obtained by solving the wave equation and a detector response correction was applied to calibrate the detected results and correct the mismatch between the measured and the real pressure signal. The practicability of this technique was demonstrated using two different laser-driven proton sources. A 9.4 MeV proton bunch (40 ns duration) produced at the MLL Tandem accelerator and attenuated to 6.2, 6.7, 7.2 and 7.8 MeV upon entering the water phantom, and a 30 MeV proton bunch (30 fs, 1 Hz repetition rate) produced by the Dresden Laser Acceleration Source (Draco) petawatt laser at Helmholtz-Zentrum Dresden-Rossendorf (HZDR). The I-BEAT algorithm calculated the expected acoustic trace to be observed by the transducer, and the results were compared to the measured curve and validated. This technique offers a high dynamic range (10^7 to 10^{11} protons/mm^2), low operation cost, compactness and robustness at high repetition rates. In addition, with this technique, no averaging or scanning is required and there is also the feasibility of 3D dose reconstruction by employing multiple transducers in several directions.

In 2016 a paper was published with the title "Ionoacoustic tomography of the proton Bragg peak in combination with ultrasound and optoacoustic imaging" [31]. This paper introduces ion-acoustic tomography (IAT) as a method for characterizing the energy distribution of an ion beam. The method is based on the detection of ultrasound waves, that are induced as the beam passes through matter, which can be inverted and used to reconstruct the dose deposition profile. The pulse lengths used were in the range of 8ns

- 9μs and pulse repetition frequency in the range of 1-10 kHz. The technique has been experimentally validated in both 2D and 3D using a 20 MeV proton beam in a water tank, where the waves have been detected using a single element transducer and a 64 element curved array transducer for each case. This technique is suitable for beams created by a laser-hybrid accelerator as it benefits from a large dynamic range and also has the ability to temporally separate the acoustic signals from the laser pulses induced by the electromagnetic pulses of the accelerator. In addition, the paper suggests a method of registering the obtained profile to the tissue morphology, by combining this ion-acoustic tomography technique with ultrasound and optoacoustic imaging. Such a hybrid system is suggested to help the optimization of the dose delivery.

In 2015, a paper was published with the title "Feasibility of RACT for 3D dose measurement and range verification in a water phantom" [32]. This paper introduces a radiation-induced acoustic computed tomography (RACT) based scanner design that can provide the integral dose and range of a pulsed proton beam in a medium. To test the scanner, a Monte Carlo simulation was performed (in FLUKA [33]) using a 206.8 MeV pulsed proton beam (1 cm lateral width, 0.776% energy spread, 27 cm Bragg peak distance). A 71-element cylindrical transducer array (0.5 mm voxel size, rotated over 2π) was used to detect the pressure signal induced by the beam in a cylindrical water phantom. 54 of the elements were positioned along the cylinder's length and 17 elements along the radius. The collection of data from several rotation angles was used to reconstruct an image using a 3D filtered back-projection method. The 3D dosimetric scanner was able to verify the proton range and dose distribution of a pencil proton beam with centi-Gray sensitivity. In addition, it was observed that the sensitivity of the scanner was influenced by the width of the beam and the bandwidth of the sensor. Comparing these results to previous experiments performed using hydrophones, it was concluded that the RACT scanner can provide an order of magnitude better sensitivity.

4.3 Ion-acoustic Studies

In 2019 a report was published with the title "Enhancement of the ionoacoustic effect through ultrasound and photoacoustic contrast agents" [34]. The report investigates the clinical benefits of using contrast agents (CA), such as ultrasound microbubbles and India ink, to enhance acoustic emissions. Specifically, ultrasound microbubbles can be used to increase the acoustic amplitude and frequency (and hence image contrast) due to a change in the shape of the ionacoustic signal, and India ink can be used to cause additional optical absorption and hence additional emissions which would enhance the signal amplitude. An experiment was performed where a 22 MeV pulsed proton beam (produced at the Tandem accelerator) was fired towards a water tank. A ripple filter made of aluminium was also used in the experimental set-up to spread-out the beam and increase its lateral dimension, due to additional scattering, and resemble more of a clinical scenario. A combination of both contrast agents has been found to increase the signal amplitude by up to 200% (MHz frequency range) compared to pure water. The paper highlights that using these (or other) contrast agents can help to overcome the detection limits in current beam diagnostics and range verification systems. Finally, the paper mentions the use of gold microbubbles and gold nanoparticles to enhance the signal dynamics and the biological effectiveness of the treatment.

In 2007 a paper was published with the title "Waveform simulation based on 3D dose distribution for acoustic wave generated by proton beam irradiation" [35]. The paper introduces a method of simulating the acoustic waveforms (pressure against time shape) produced when a pulsed proton beam is absorbed by a medium. The method is based on Green function transmission models and the assumption that the heat rate is proportional to the dose distribution. Using this model, the acoustic waveform was calculated from 3D dose distribution data. To verify the simulated model, an experiment was performed using a 230 MeV pulsed proton beam (50 ns width and 50 ms interval) propagating through a water tank. An imaging plate has been inserted in the water, which enabled the 2D dose distribution to be obtained from the detected pressure. The 3D distribution was then calculated from the 2D data using a modulated quenching factor. The calculated acoustic waveform shape obtained from the experiment was compared to the results of the simulation and they are in close agreement. This verifies that the model works and that the time structure of the pressure waves can be obtained from the 3D dose distribution.

4.4 Bragg Peak Localization Studies

In 1997, a paper was published with the title "An analytical approximation of the Bragg curve for therapeutic proton beams" [36]. The paper provides a model for the analytical approximation of the Bragg peak curve based on the measured data, using a parabolic cylinder and Gaussian functions, rather than a purely mathematical approach which cannot be generalized. The model was compared to numerically calculated data from dose calculation algorithms as well as compared to measured data provided by several proton centers. The model was verified for the 10-200 MeV protons range. The full analytical representation can enable the extrapolation of the measured data and allow more accurate dose calculations when it comes to clinical applications.

In 2015, a paper was published with the title "Ionoacoustic characterization of the proton Bragg peak with submillimeter accuracy" [37]. This paper investigates the resolution of ionacoustic tomography for providing range verification of ions in tissue. The dose distribution of protons in water was simulated in Geant4 and the acoustic wave generation and propagation in k-Wave. An experiment has also been performed using a water tank, a pulsed 20 MeV proton beam (8 ns—4.3 μs width, 3 ns rise time, 1—10 kHz repetition frequency) produced at the Tandem accelerator and an ultrasound transducer on-axis with the beam. The length and pulse intensity were varied, as well as used different piezo-composite transducers to observe their effect on the range verification accuracy. It was found that energy depositions as low as 10^{12} eV could be measured and that the Bragg peak could be localized within 30 μm. It was also observed that an increase in the number of particles per pulse resulted in a linear signal amplitude increase. In addition, it was observed that there is a linear signal dependence on the delivered dose. It was also observed that for proton pulse widths above 200 ns, there is a linear relationship between the positive-negative peak distance and the width of the pulse. Simulations with 150 MeV proton beam also revealed the advantage of having larger amplitudes and hence more promising ionacoustic range verification for clinically relevant proton beam.

5 Method

5.1 Designing and Simulating the SmartPhantom

To mimic the human body, a SmartPhantom has been simulated in Geant4. The simulated phantom is a 30 cm × 30 cm × 30 cm box filled with water, with the walls surrounding it made of plexiglass (10 mm thickness). Scintillating fibre planes have also been simulated and inserted within it, where each one is composed of 492 polystyrene scintillating fibres (250 μm diameter) and epoxy resin to keep them in place and act as glue. Two such planes have been placed perpendicular to each other to allow results to be obtained in 2D. A 6.5 cm × 6.5 cm window has also been simulated on one side of the box (6.95 mm plexiglass thickness) to act as an entrance for the beam. A figure of the simulated SmartPhantom is shown in Figure 5. This simulation has been created by another member of the group.

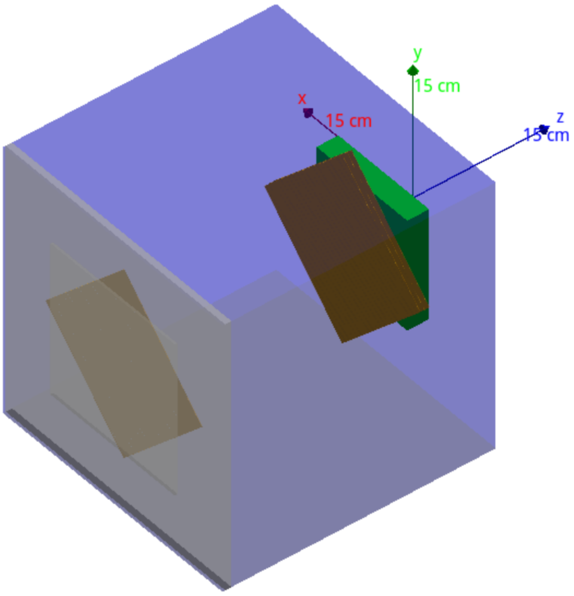

Figure 5. An illustration of the SmartPhantom simulated in Geant4. The blue area indicates water and the brown cuboids represents the scintillating fibre planes.

The energy deposition data produced while the beam propagates through the water tank have been written in a C++ file that is compatible with the k-Wave software. This was done by voxalising the phantom into small segments and storing the time-varying energy data in each one.

5.2 Simulating the ion-acoustic Process

The time-varying energy output from Geant4 was used as the source acoustic input into k-Wave, to simulate the ion energy transfer to the medium, the generation of the acoustic waves and their propagation in the three-dimensional space until detection. To do this, the initial pressure distribution, $p_0(\mathbf{r},T)$, was calculated from the Geant4 output energy distribution, $D(\mathbf{r},T)$, using Equation 5.1, where Γ is the dimensionless Grüneisen coefficient and $\rho(\mathbf{r},T)$ the target mass density [24]. The Grüneisen coefficient is a measure of the efficiency when converting between the absorbed heat energy and the induced pressure, and is calculated using Equation 5.2, where c is the speed of sound in the medium, β the thermal expansion coefficient and C_p the specific heat capacity [22]. For water at room temperature, this value is approximately 0.11 [22].

$$p_0(\mathbf{r},T) = \Gamma(\mathbf{r},T) \times D(\mathbf{r},T) \times \rho(\mathbf{r},T) \tag{5.1}$$

$$\Gamma(\mathbf{r},T) = \frac{c^2\beta}{C_p} \tag{5.2}$$

Once the initial pressure distribution was obtained, the temperature rise, pressure rise and the propagation of the compressional waves through the medium are simulated in the time-domain in Cartesian coordinates using k-Wave's "kspaceFirstOrder3D()" function. This function takes the sensor, speed of sound in the medium (1500 m/s in the case of water), source point, grid dimensions and timestep as arguments. A time-step equal to $\frac{N_x dx}{c}$ was used, where N_x is the number of voxels, c is the speed of sound in the medium and dx is the width of each voxel. An isotropic absorbing boundary layer was also implemented in the simulation to enclose the generated waves and prevent them from escaping one side of the domain and reappearing on the opposite side.

5.3 Acoustic Sensor Design & Detection

Initially, a planar sensor was simulated to test the ability to detect and reconstruct the pressure distribution from the source. As a second step, the shape was changed to a hemisphere, to resemble more of a real transducer, centered in the middle of the x-y plane. The sensor was composed of several voxels where each one acted as a single element and the signal received by each one were summed to give a total sensor signal. This hemispherical sensor shape was created using k-Wave's *makeBowl()* function [20] and it has several advantages compared to a planar sensor, including a wider field-of-view and elimination of directional dependence in the response. This was verified by the fact that better reconstructed images were obtained.

When confirmed that the hemispherical sensor shape is able to provide a good pressure reconstruction, a sensor consisting of an array of evenly distributed disk elements has been developed using k-Wave's *kWaveArray* class [20]. The function uses an off-grid approach so that elements smaller than the size of one grid can be implemented in the simulation. This class supports elements of different shapes and sizes, and the signals from each element can added to give a single combined signal from the whole sensor.

To create evenly distributed elements lying on the surface of the hemisphere, a golden spiral array design has been developed which uses a Fibonacci lattice to calculate the elements' position [38]. An example of the location of 500 elements lying on the surface of a 0.06 m radius sphere is shown in Figure 6.

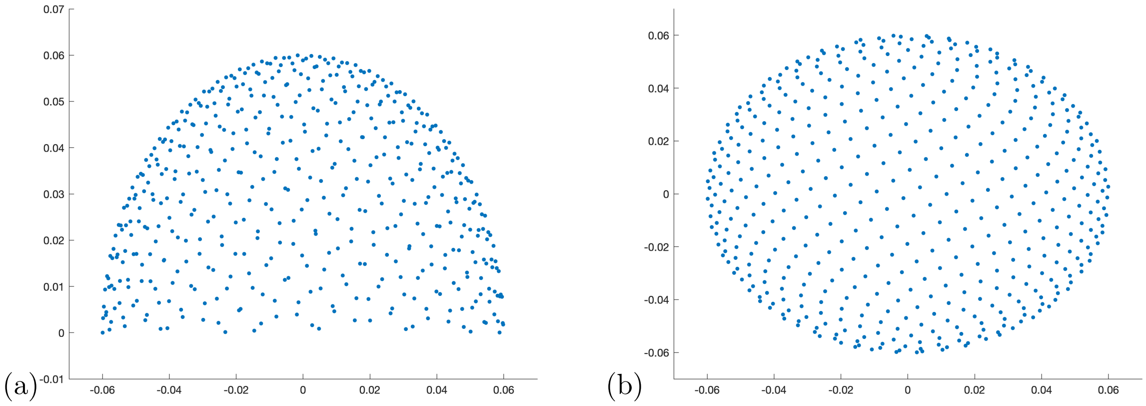

Figure 6. Hemispherical sensor array with 500 disk elements arranged on the surface in a golden spiral pattern: (a) side view and (b) top view.

The time-dependent pressure detected at each element was obtained and the total acoustic pressure field was computed from the values. From the data, the dose deposition image was reconstructed with higher pixel intensity indicating high-pressure regions. The image reconstruction was performed using several different methods that are discussed in Section 5.4.

5.4 Performing Image Reconstruction

Three different image reconstruction techniques have been performed to obtain the pressure distribution of the incoming beam within the simulated water tank. These are time-reversal, model-based minimization and back-projection. The results obtained from each one can then be compared to see which one gives the best estimate of the Bragg peak.

5.4.1 Time Reversal Reconstruction

A single time-reversal (TR) reconstruction can be performed in four steps. Initially, the time-varying acoustic field generated by the source is measured by the sensor and stored. Then, the measured signals at each element are time-reversed and, subsequently, each element acts as a source point that emits these time-reversed signals. These emitted signals then propagate back to the original source where they interfere constructively and an image can be formed [39]. Time-reversal can be achieved in k-Wave by using the *sensor.time_reversal_boundary_data*() function which can take the measured data at the sensor location as input and time-reverse them. In addition, time reversal reconstruction works because the wave equation is invariant under time transformation, T: t $\rightarrow -t$.

The time-reversal method can also be iterated to improve the reconstruction. This can be done by subtracting the first reconstruction time-series from the original time-series to calculate a residual. Then, this residual can be used to form an image, using the time-reversal method, and then add this image to the original image to give an improved estimate. After performing N iterations, the reconstructed pressure distribution is given by the expression $p_0^{(N)} = p_0^{(N-1)} + p_r^{(N-1)}$, where p_r is the pressure distribution calculated from the residual signals [39]. Iterations can be performed until there is no noticeable improvement.

5.4.2 Model-based Minimisation Reconstruction

In the model-based minimisation reconstruction method, the difference in the time-series when the measured signal is subtracted from the modelled data is used as a source point for the model. This method is very similar to the iterative time reversal, but instead of replacing the data at each point in time, the data are added to the existing field [20]. The update in each iteration reduces the loss function (difference between current and expected output) that the iterations are trying to minimize. This method has the advantage of incorporating a regularisation into the iterations thereby allows good reconstructions with sparse or limited data.

5.4.3 Filtered Back-projection Reconstruction

The back-projection reconstruction method essentially back-projects the data from the receiver point back to the object plane [40]. By having multiple sensor elements positioned at different angles around the object, the back-projected data from each one can be collected and used to form an image. Generally, the more the angles the better the reconstructed image. A drawback of this method is that for angles where there is no element to collect data from, the corresponding area will appear blurred. To remove this blurring, a filter can be applied. Such a filter can accentuate high frequencies and minimize low frequencies to produce a smoother image. Generally, back-projection is much faster than other methods since no iterations are needed.

6 Preliminary Results & Analysis

6.1 Image Reconstruction Results

All of the following results come from the energy depositions of a 200 MeV proton beam (10^4 protons) propagating through a water phantom that was simulated in Geant4, as discussed in Section 5.1. The simulated phantom has been split into several voxels and the energy deposition in each one has been saved into a file and imported in Matlab to perform the image reconstruction techniques discussed in Section 5.4.

Both the initial (imported) and reconstructed energy distribution profiles along the beam direction of propagation have been parameterised by fitting the data with an analytical approximation of the Bragg peak curve. This curve is shown in Equation 6.1 [36] and is valid for proton beams with energies between 10 and 200 MeV, travelling through water. In this equation Φ_0 is the fluence, σ is the standard deviation, p is the exponent of the range-energy relation, Γ is the fraction of the energy released in nuclear interactions, ρ is the water density in g/cm^3, a is a proportionality factor, β is the slope parameter of the fluence reduction relation, R_0 is the range, γ is the fraction of the energy released, ϵ is the fraction of the fluence contributing to the 'tail' of the energy spectrum, $\mathfrak{D}$ is the parabolic cylinder function and $\zeta = \frac{R_0 - z}{\sigma}$ where z is the position along the z-axis.

$$D_{H_20}(z) = \Phi_0 \frac{e^{\frac{-\zeta^2}{4}} \sigma^{\frac{1}{p}} \Gamma(1/p)}{\sqrt{2\pi} \rho p a^{\frac{1}{p}} (1 + \beta R_0)} [\frac{1}{\sigma} \mathfrak{D}_{\frac{-1}{p}}(-\zeta) + (\frac{\beta}{p} + \gamma\beta + \frac{\epsilon}{R_0}) \mathfrak{D}_{\frac{-1}{p-1}}(-\zeta)] \qquad (6.1)$$

The k-Wave simulation has been split into 5 mm square voxels, to match the Geant4 input. The sensor array used to collect data and perform image reconstruction has been designed using the method explained in Section 5.3, and it consists of 250 disk elements, 2 mm diameter each, and has a radius of 10 cm. The sensor design and position with respect to the beam in the water tank is shown in Figure 7. The location and size have been chosen in such a way that it can fit into the tank and also be as close to the Bragg peak. Convergence tests have been performed to examine the effect of varying several parameters and observe their impact on the image reconstruction accuracy.

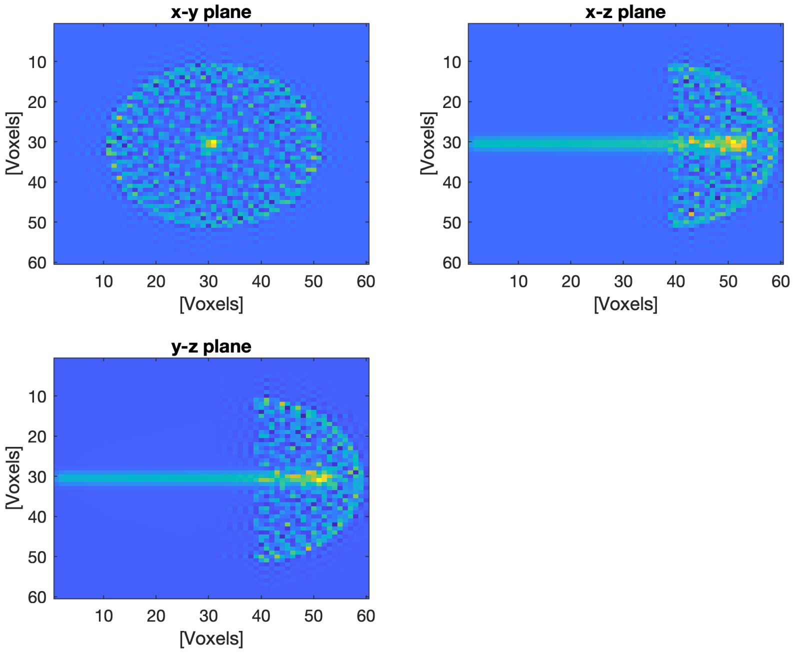

Figure 7. Hemispherical sensor array with elements evenly distributed along the surface. The sensor consists of 250 disk elements, 2 mm diameter each, and has a radius of 10 cm. The sensor has been designed in k-Wave and its position relative to the propagating proton beam within the water tank is shown.

6.1.1 Time Reversal Reconstruction

Time-reversal reconstruction has been performed as explained in Section 5.4.1. The time-reversal reconstruction has also been iterated to obtain an improved estimate of the reconstructed pressure distribution. The results after 6 time-reversal iterations are shown in Figure 8. The results of fitting the analytical approximation curve to the data are shown in Figure 9. From both figures it can be seen that there is a Bragg peak along the direction of the beam propagation within the water tank, as expected. It can also be seen that as the number of time-reversal iterations increases, the better the reconstructed pressure. Furthermore, it can be seen that there is a poor reconstruction of the tail. This can be explained due to the position of the sensor which is closer to the Bragg peak and far away from the tail, hence not much data can be collected from that region. It is expected that increasing the radius of the sensor would give a better reconstruction in that area. In addition, from these figures, it can be seen that after 6 iterations the values converge and it no longer improves the estimate.

The reconstructed pressure distribution along all planes, compared to the initial pressure distribution as imported from Geant4, after 6 time-reversal image reconstruction iterations is shown in Figure 10. As expected, there is poor pressure reconstruction around the tail of the beam and a good reconstruction around the Bragg peak.

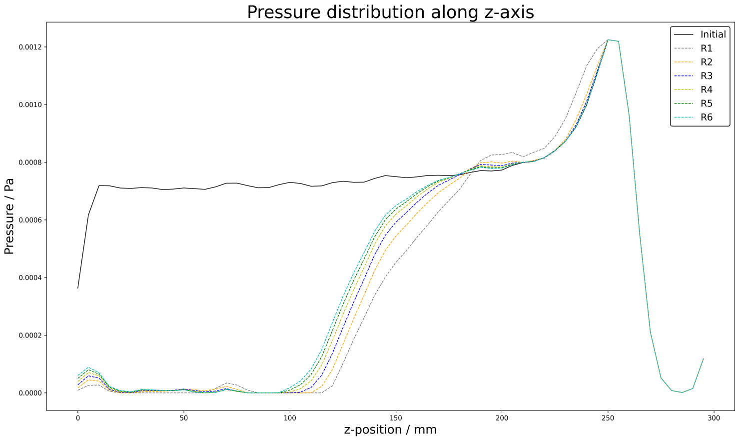

Figure 8. Initial and reconstructed pressure distribution along the beam propagation axis using the time-reversal method. Each colour corresponds to different iterations number.

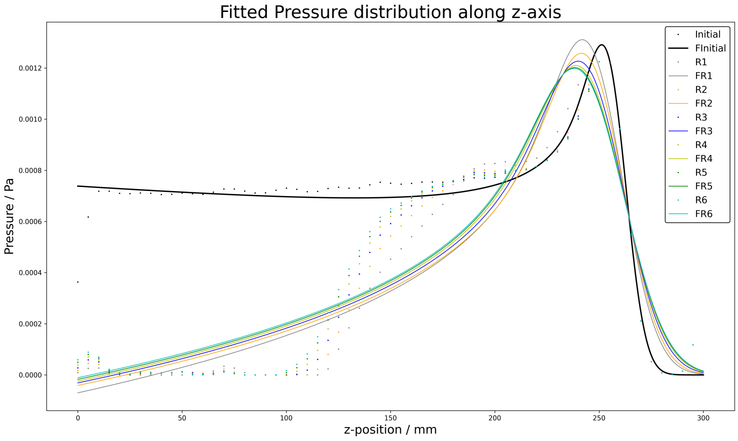

Figure 9. Initial and reconstructed pressure distribution along the beam propagation axis using the time-reversal method. Points indicate the output of the simulation and lines indicated the fitted curves.

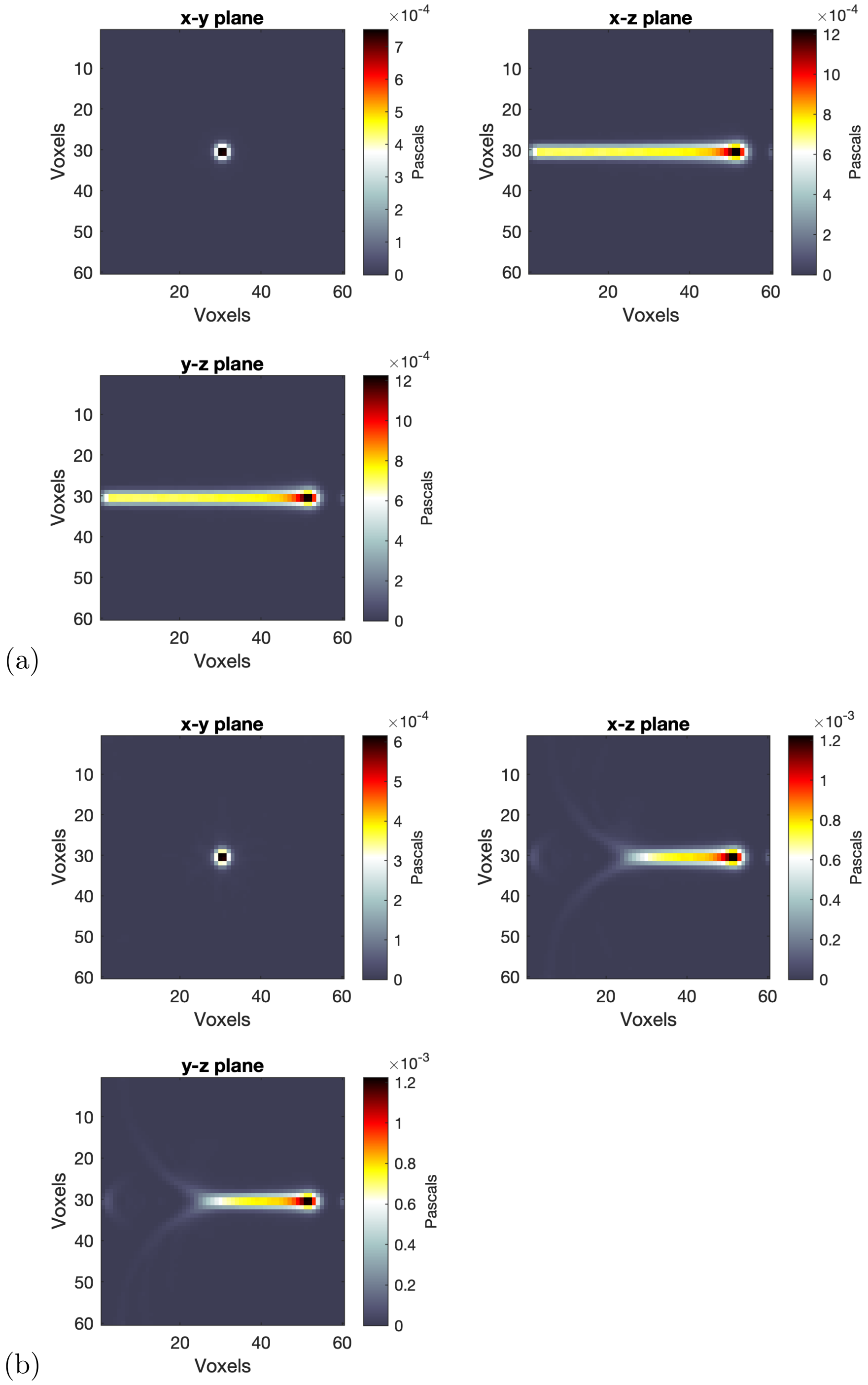

Figure 10. (a) Initial pressure distribution. (b) Reconstructed pressure distribution after 6 iterations of time-reversal image reconstruction. The Figures have been created in k-Wave.

6.1.2 Model-based Minimization Reconstruction

Model-based minimization reconstruction has been performed as explained in Section 5.4.2. The reconstruction has been improved by performing multiple iterations. The results of the pressure distribution along the z-axis are shown in Figure 11 and the fitted analytical approximation is shown in Figure 12. The reconstructed pressure distribution in the three planes is shown in Figure 13.

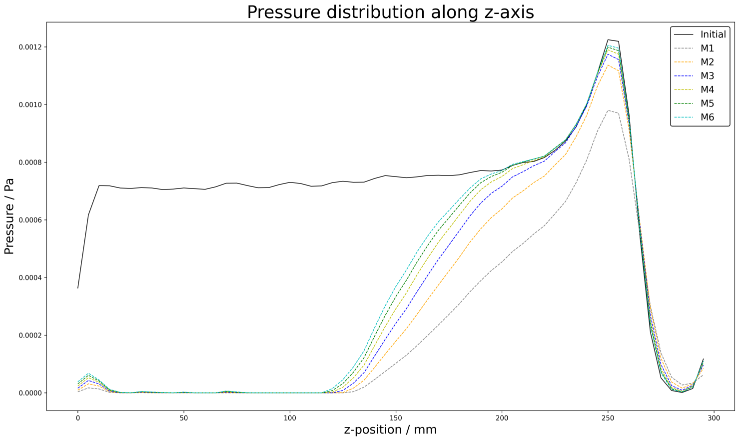

Figure 11. Initial and reconstructed pressure distribution along the beam propagation axis using the model-based minimization method. Each colour corresponds to different iterations number.

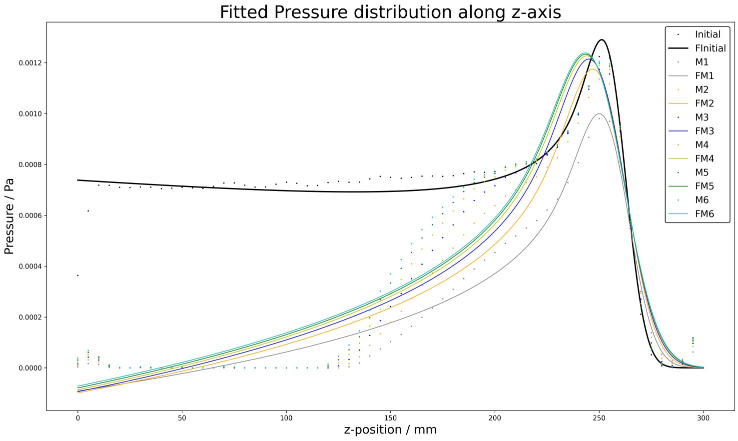

Figure 12. Initial and reconstructed pressure distribution along the beam propagation axis using the model-based minimization method. Points indicate the output of the simulation and lines indicated the fitted curves.

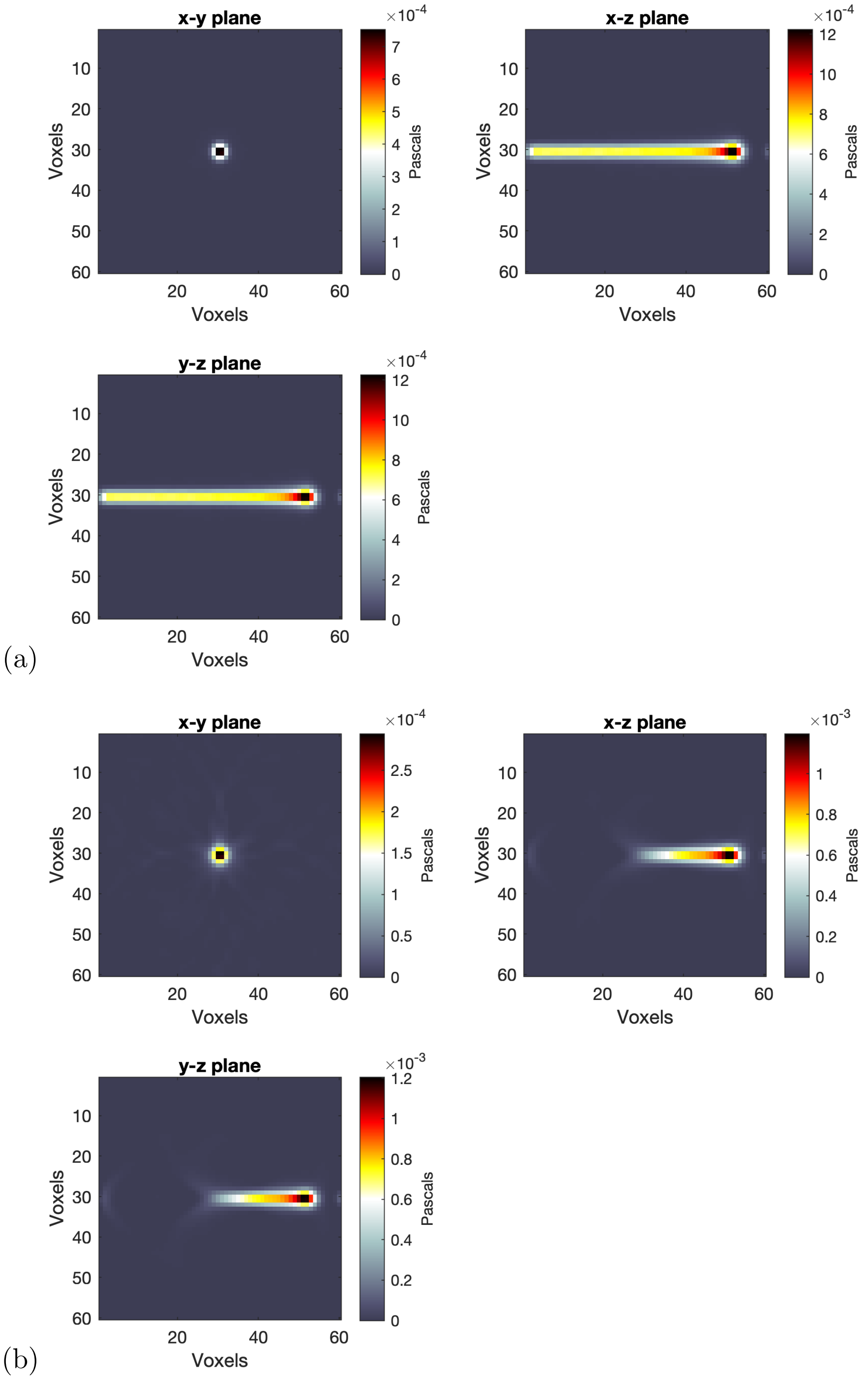

Figure 13. (a) Initial pressure distribution. (b) Reconstructed pressure distribution using 6 iterations of the model-based minimization image reconstruction. The Figures have been created in k-Wave.

From these graphs, it can be seen that there is a poor reconstruction of the tail, which is even less accurate than using the time-reversal method. In addition, as the number of iterations increases, the reconstruction of the Bragg peak gets better. The reconstruction is still less accurate than the time-reversal reconstruction for the same number of iterations and detector specifications.

6.1.3 Back-projection Reconstruction

As a third method, the back-projection image reconstruction has been performed, as explained in Section 5.4.3. This method is much faster compared to the other two since no iterations are made. The results of the pressure distribution along the direction of propagation compared to the initial distribution are shown in Figure 14 and the results after fitting the analytical curve to the data is shown in Figure 15. The image reconstruction in the three planes is shown in Figure 16. From both figures, it can be seen that the 'tail' of the beam cannot be reconstructed. This is mainly because the area of the detector doesn't cover that part of the beam therefore no back-projected data can be collected. It can also be seen that there is poor image reconstruction along the x-y plane. This is expected to become better with more, closely-spaced and larger detector elements.

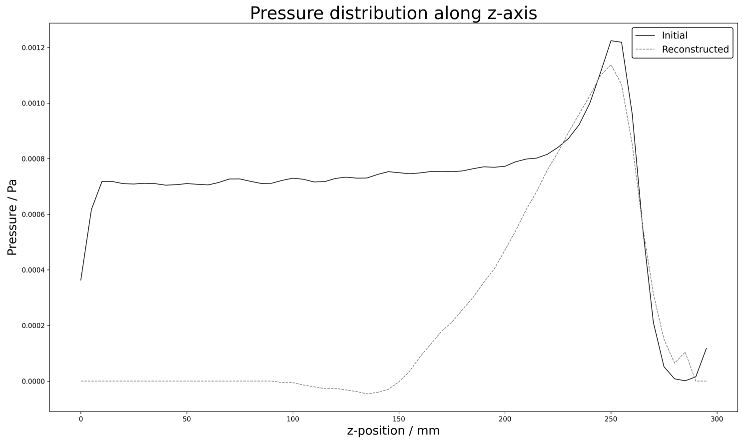

Figure 14. Initial and reconstructed pressure distribution along the beam propagation axis using the back-projection method.

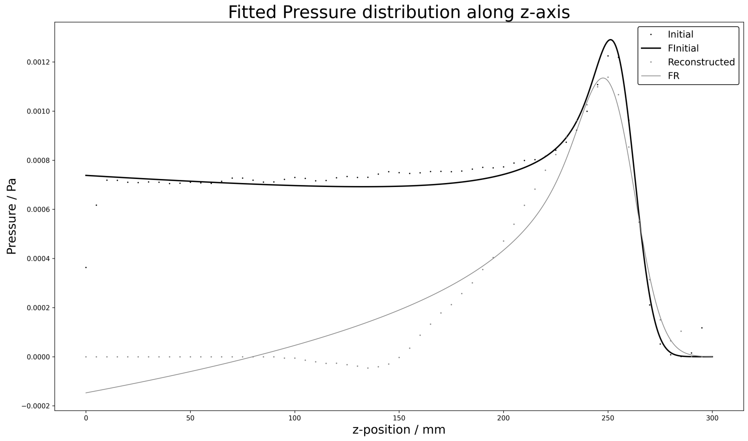

Figure 15. Initial and reconstructed pressure distribution along the beam propagation axis using the back-projection method. Points indicate the output of the simulations and lines indicated the fitted curves.

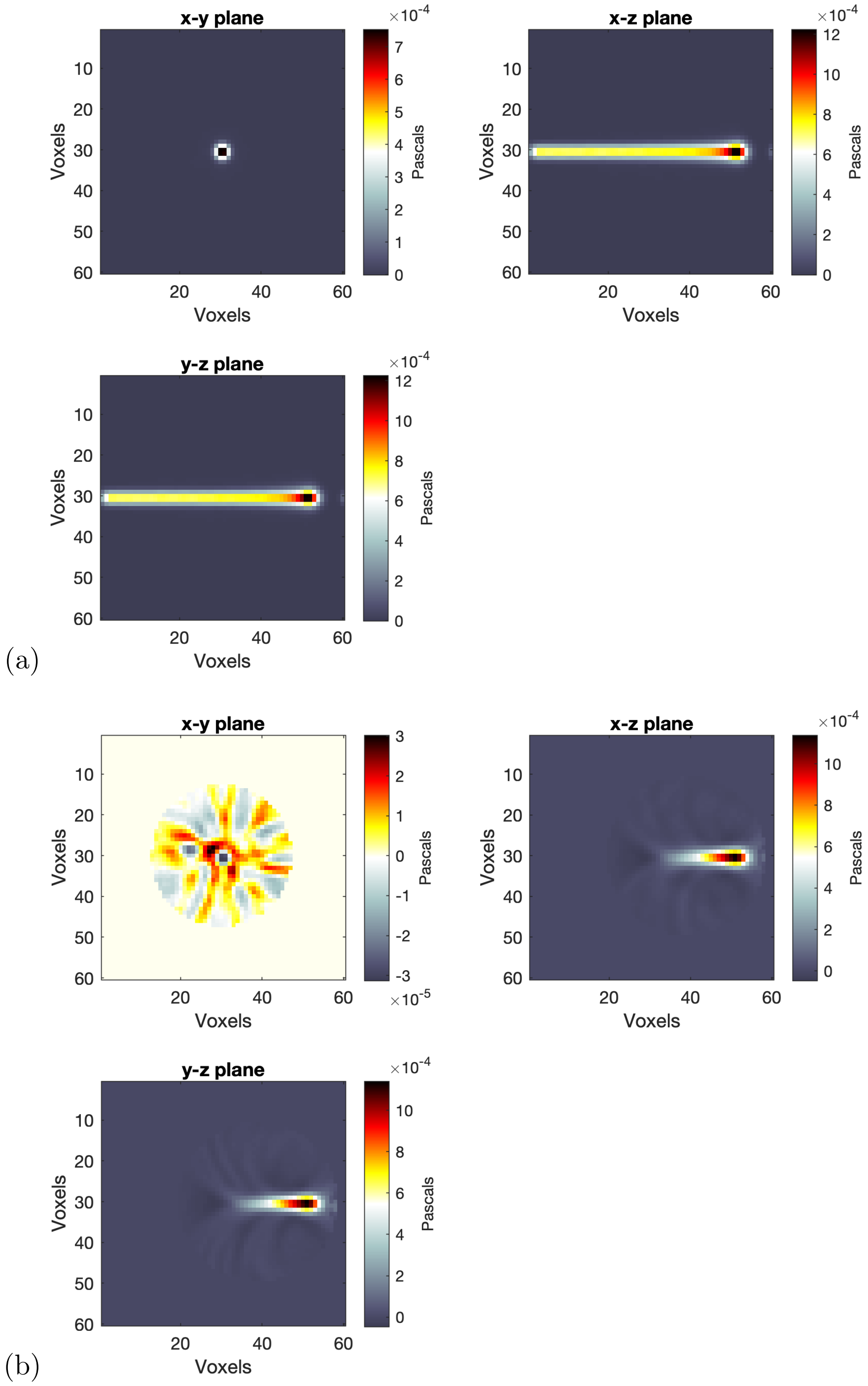

Figure 16. (a) Initial pressure distribution. (b) Reconstructed pressure distribution using the back-projection method. The Figures have been created in k-Wave.

7 Discussion & Future Work

Radiotherapy is an effective, non-invasive way of treating tumours. Ions are considered to be more effective than photons because they deposit most of their energy in a small volume of tissue rather than along the entire path of the beam from the surface to the tumour. This is advantageous because it minimizes the radiation received by the surrounding healthy cells which can damage them and cause further tumours to develop. Because of this, the accurate localization of the Bragg peak (maximum dose accumulation) is extremely important. This localization can be achieved using medical imaging techniques, especially, ion-acoustic imaging which is a promising technique to reconstruct the dose deposition profile using ultrasound pulses. Ion-acoustic imaging has several advantages, including good resolution and large penetration depth.

Ion-acoustic imaging has been used to perform image reconstructions of a 200 MeV proton beam travelling through a water phantom, which acts as a proof-of-principle experiment for LhARA as it can effectively mimic human muscle and soft tissue. The energy as a function of distance output from a Geant4 water phantom simulation has been used as a source input in k-Wave to reconstruct the images and obtain the pressure deposition profile. Three different image reconstruction techniques have been investigated: time-reversal, model-based minimization and back-projection. This was done by collecting the pressure data arriving at a hemispherical sensor array with 250 evenly distributed elements lying on its surface.

The iterative time-reversal reconstruction is the best reconstruction technique as after approximately 6 iterations the reconstructed pressure distribution along the energy of beam propagation is in very close agreement with the initial distribution. The 3D pressure distribution reconstruction also has very few artefacts around the tail of the beam, while the Bragg peak is reconstructed with good accuracy. The model-based minimization reconstruction is also able to reconstruct the Bragg peak but there is still some discrepancy between the reconstruction and the Bragg peak from the initial distribution. This might be corrected when more iterations are used. In addition, the tail of the beam is not reconstructed as well as with the time-reversal method. Finally, the back-projection reconstruction is the fastest and appears to give a relatively good reconstruction of the Bragg peak for the same sensor specifications. The reconstruction though is not as good as the other two techniques, but it is expected that better results would be obtained when more and larger elements are used in the sensor array.

With regards to future work, additional tests on the radius and the position of the detector need to be made to determine the best size and position to locate the sensor array in order to obtain the best results. Furthermore, to design the sensor specifications for the real experiment, the number of elements as well as their size also need to be examined. Ways also need to be found in order to make the reconstructions fast enough to allow real-time monitoring of the Bragg peak. As an additional step, machine learning can also be implemented in the reconstructed images which can potentially improve both the speed and the reconstruction accuracy.

Finally, when the proof-of-principle experiment is validated using the simulations, and when the best reconstruction method and sensor specification are obtained, the real experiment can be performed. The SmartPhantom, scintillating fibre planes and sensor need to be constructed and tested with a real 200 MeV proton beam, to validate the whole system.

References

[1] World Health Organization: WHO (2019). Cancer. [online] Who.int. Available at: https://www.who.int/health-topics/cancertab=tab_1.

[2] Cancer Research UK. (2019). Worldwide cancer statistics. [online] Available at: https://www.cancerresearchuk.org/health-professional/cancer-statistics/worldwide-cancer.

[3] Cancerresearchuk.org. (2018). Radiotherapy | Cancer in general | Cancer Research UK. [online] Available at: https://www.cancerresearchuk.org/about-cancer/cancer-in-general/treatment/radiotherapy [Accessed 8 Feb. 2022].

[4] Cancer.net. (2019). Understanding Radiation Therapy. [online] Available at: https://www.cancer.net/navigating-cancer-care/how-cancer-treated/radiation-therapy/understanding-radiation-therapy [Accessed 8 Feb. 2022].

[5] Lehrer EJ, Prabhu AV, Sindhu KK, Lazarev S, Ruiz-Garcia H, Peterson JL, Beltran C, Furutani K, Schlesinger D, Sheehan JP, Trifiletti DM. Proton and Heavy Particle Intracranial Radiosurgery. Biomedicines. 2021 Jan 3;9(1):31. doi: 10.3390/biomedicines9010031. PMID: 33401613; PMCID: PMC7823941.

[6] Nrc.gov. (2019). NRC: Glossary – Gray (Gy). [online] Available at: https://www.nrc.gov/reading-rm/basic-ref/glossary/gray-gy.html.

[7] W. R. Leo. Techniques for Nuclear and Particle Physics Experiments. Springer- Verlag Berlin Heidelberg, 1987.

[8] www.britannica.com. (n.d.). radiation - Stopping power | Britannica. [online] Available at: https://www.britannica.com/science/radiation/Stopping-power [Accessed 23 Mar. 2022].

[9] www.sciencedirect.com. (n.d.). Relative Biologic Effectiveness - an overview | ScienceDirect Topics. [online] Available at: https://www.sciencedirect.com/topics/biochemistry-genetics-and-molecular-biology/relative-biologic-effectiveness.

[10] ResearchGate (2011). Typical RBE values for different radiation qualities. [online] Available at: https://www.researchgate.net/figure/1-Typical-RBE-values-for-different-radiation-qualities_tbl1_308722052 [Accessed 23 Mar. 2022].

[11] Center for Devices and Radiological Health (2018). Medical Imaging. [online] U.S. Food and Drug Administration. Available at: https://www.fda.gov/radiation-emitting-products/radiation-emitting-products-and-procedures/medical-imaging.

[12] Richards, A.A. (n.d.). Acoustic Imaging: Seeing with Sound. Alien Vision: Exploring the Electromagnetic Spectrum with Imaging Technology.

[13] Barrie Smith, N. and Webb, A. (n.d.). Introduction to Medical Imaging. Cambridge University Press, pp.42-45, 145–157, 178-179.

[14] Beard, P., 2011. Biomedical photoacoustic imaging. Interface Focus, 1(4), pp.602-631.

[15] Anon, (n.d.). Review of Cost Reduction Methods in Photoacoustic Computed Tomography. [online] Available at: https://arxiv.org/pdf/1902.09987.pdf [Accessed 24 Mar. 2022].

[16] LhARA: The Laser-hybrid Accelerator for Radiobiological Applications. (2020). Frontiers in Physics. [online] Available at: https://www.frontiersin.org/articles/10.3389/fphy.2020.567738/full [Accessed 18 Feb. 2022].

[17] Hughes, J.R. and Parsons, J.L. (2020). FLASH Radiotherapy: Current Knowledge and Future Insights Using Proton-Beam Therapy. International Journal of Molecular Sciences, 21(18), p.6492.

[18] CERN. 2020. User Documentation. [online] Available at: https://geant4.web.cern.ch/support/user_documentation. [Accessed 18 Apr. 2022].

[19] nl.mathworks.com. (n.d.). MATLAB - MathWorks. [online] Available at: https://nl.mathworks.com/products/matlab.html.

[20] www.k-wave.org. (n.d.). k-Wave: A MATLAB toolbox for the time domain simulation of acoustic wave fields. [online] Available at: http://www.k-wave.org [Accessed 19 Mar. 2022].

[21] Treeby, B.E., Jaros, J., Rendell, A.P. and Cox, B.T. (2012). Modeling nonlinear ultrasound propagation in heterogeneous media with power law absorption using a k-space pseudospectral method. The Journal of the Acoustical Society of America, [online] 131(6), pp.4324–4336. Available at: https://pubmed.ncbi.nlm.nih.gov/22712907/ [Accessed 19 Mar. 2022].

[22] Jones KC, Nie W, Chu JCH, et al. Acoustic-based proton range verification in heterogeneous tissue: simulation studies. Phys Med Biol. 2018;63(2):025018. Published 2018 Jan 11. doi:10.1088/1361-6560/aa9d16

[23] www.varian.com. (n.d.). Eclipse | Varian. [online] Available at: https://www.varian.com/en-gb/products/radiotherapy/treatment-planning/eclipse.

[24] Freijo C, Herraiz JL, Sanchez-Parcerisa D, Udias JM. Dictionary-based protoacoustic dose map imaging for proton range verification. Photoacoustics. 2021 Jan 16;21:100240. doi: 10.1016/j.pacs.2021.100240. PMID: 33520652; PMCID: PMC7820918.

[25] Patch SK, Hoff DEM, Webb TB, Sobotka LG, Zhao T. Two-stage ionoacoustic range verification leveraging Monte Carlo and acoustic simulations to stably account for tissue inhomogeneity and accelerator-specific time structure - A simulation study. Med Phys. 2018 Feb;45(2):783-793. doi: 10.1002/mp.12681. Epub 2017 Dec 21. PMID: 29159885.

[26] Yu Y, Li Z, Zhang D, Xing L, Peng H. Simulation studies of time reversal-based protoacoustic reconstruction for range and dose verification in proton therapy. Med Phys. 2019 Aug;46(8):3649-3662. doi: 10.1002/mp.13661. Epub 2019 Jul 5. PMID: 31199511.

[27] opengate.readthedocs.io. (n.d.). Introduction — GATE documentation. [online] Available at: https://opengate.readthedocs.io/en/latest/introduction.html [Accessed 7 Jun. 2022].

[28] Jones KC, Vander Stappen F, Sehgal CM, Avery S. Acoustic time-of-flight for proton range verification in water. Med Phys. 2016 Sep;43(9):5213. doi: 10.1118/1.4961120. PMID: 27587053.

[29] Vallicelli, Elia Cosmi, Mattia Baschirotto, Andrea De Matteis, Marcello. (2021). Front-end Design Optimization for Ionoacoustic 200 MeV Protons Beam Monitoring with Sub-millimeter Precision for Hadron Therapy Applications. 77-87. 10.5220/0010346600770087.

[30] Haffa D, Yang R, Bin J, Lehrack S, Brack FE, Ding H, Englbrecht FS, Gao Y, Gebhard J, Gilljohann M, Götzfried J, Hartmann J, Herr S, Hilz P, Kraft SD, Kreuzer C, Kroll F,

Lindner FH, Metzkes-Ng J, Ostermayr TM, Ridente E, Rösch TF, Schilling G, Schlenvoigt HP, Speicher M, Taray D, Würl M, Zeil K, Schramm U, Karsch S, Parodi K, Bolton PR, Assmann W, Schreiber J. I-BEAT: Ultrasonic method for online measurement of the energy distribution of a single ion bunch. Sci Rep. 2019 Apr 30;9(1):6714. doi: 10.1038/s41598-019-42920-5. PMID: 31040311; PMCID: PMC6491586.

[31] Kellnberger S, Assmann W, Lehrack S, Reinhardt S, Thirolf P, Queirós D, Sergiadis G, Dollinger G, Parodi K, Ntziachristos V. Ionoacoustic tomography of the proton Bragg peak in combination with ultrasound and optoacoustic imaging. Sci Rep. 2016 Jul 7;6:29305. doi: 10.1038/srep29305. PMID: 27384505; PMCID: PMC4935843.

[32] Alsanea F, Moskvin V, Stantz KM. Feasibility of RACT for 3D dose measurement and range verification in a water phantom. Med Phys. 2015 Feb;42(2):937-46. doi: 10.1118/1.4906241. PMID: 25652506.

[33] www.fluka.org. (n.d.). The official FLUKA site: FLUKA home. [online] Available at: http://www.fluka.org/fluka.php [Accessed 7 Jun. 2022].

[34] Lascaud J, Dash P, Würl M, Wieser HP, Wollant B, Kalunga R, Assmann W, Clevert DA, Ferrari A, Sala P, Savoia AS, Parodi K. Enhancement of the ionoacoustic effect through ultrasound and photoacoustic contrast agents. Sci Rep. 2021 Feb 1;11(1):2725. doi: 10.1038/s41598-021-81964-4. PMID: 33526802; PMCID: PMC7851171.

[35] Terunuma T, Sakae T, Hayakawa Y, Nohtomi A, Takada Y, Yasuoka K, Maruhashi A. Waveform simulation based on 3D dose distribution for acoustic wave generated by proton beam irradiation. Med Phys. 2007 Sep;34(9):3642-8. doi: 10.1118/1.2767985. PMID: 17926968.

[36] Bortfeld T. An analytical approximation of the Bragg curve for therapeutic proton beams. Med Phys. 1997 Dec;24(12):2024-33. doi: 10.1118/1.598116. PMID: 9434986.

[37] Assmann W, Kellnberger S, Reinhardt S, Lehrack S, Edlich A, Thirolf PG, Moser M, Dollinger G, Omar M, Ntziachristos V, Parodi K. Ionoacoustic characterization of the proton Bragg peak with submillimeter accuracy. Med Phys. 2015 Feb;42(2):567-74. doi: 10.1118/1.4905047. PMID: 25652477.

[38] Anon, (n.d.). How to evenly distribute points on a sphere more effectively than the canonical Fibonacci Lattice | Extreme Learning. [online] Available at: http://extremelearning.com.au/how-to-evenly-distribute-points-on-a-sphere-more-effectively-than-the-canonical-fibonacci-lattice/.

[39] Huang, Chao et al. “Full-wave iterative image reconstruction in photoacoustic tomography with acoustically inhomogeneous media.” IEEE transactions on medical imaging vol. 32,6 (2013): 1097-110. doi:10.1109/TMI.2013.2254496

[40] www.sciencedirect.com. (n.d.). Backprojection - an overview | ScienceDirect Topics. [online] Available at: https://www.sciencedirect.com/topics/engineering/backprojection.